Refining anodic and cathodic dissolution mechanisms: combined AESEC-EIS applied to Al-Zn pure phase in alkaline solution

Junsoo Han, Vincent Vivier, Kevin Ogle

Refining anodic and cathodic dissolution mechanisms: Combined AESEC-EIS applied to Al-Zn pure phase in alkaline solution

Junsoo Han[a, c, *], Vincent Vivier[b] and Kevin Ogle[a]

[a] Chimie ParisTech, PSL Research University, CNRS, Institut de Recherche Chimie Paris (IRCP), F-75005 Paris, France
[b] Sorbonne Université, CNRS, Laboratoire Interfaces et Systèmes Electrochimiques, LISE, F-75005, Paris, France
[c] Present address: Department of Materials Science and Engineering, University of Virginia, Charlottesville, VA 22904, United States
[*]: corresponding author

Abstract

In this work, the use of atomic emission spectroelectrochemistry (AESEC) coupled to electrochemical impedance spectroscopy (EIS) is presented as a method of revealing dissolution mechanisms. To illustrate the method, the dissolution kinetics of Al cations from an Al-Zn pure phase (Zn-68 wt.% Al) was investigated in an alkaline solution. In the cathodic potential domain, a nearly direct formation of dissolved Al^{3+} was observed, while in the anodic potential domain the Al dissolution occurred by migration across a $ZnO/Zn(OH)_2$ film. The localization of the charge transfer mechanism depending on applied potential could be distinguished by comparing the DC and AC faradaic yield using AESEC-EIS.

Introduction

Since its introduction to the corrosion field by Epelboin *et al*. [1], electrochemical impedance spectroscopy (EIS) has proven itself an essential and ubiquitous technique in corrosion research. For steady state corroding systems, the EIS spectrum may in some cases be used to estimate the corrosion rate of the material without significant electrochemical perturbation of the system [1], and the EIS spectrum itself is often considered as a fingerprint for specific mechanisms revealing different kinetic processes over a wide range of time constants [2]. The difficulty of EIS alone is the inability to identify the specific faradaic reactions that occur during charge transfer. This has given rise to the development of a variety of couplings such as EIS – Raman spectroscopy [3]. The modulated Raman emission signal allows one to "tune in" to surface chemical bonds that form and dissipate in resonance with the modulated electrochemical potential. The theoretical development of such techniques has been addressed in the development of a generalized EIS transfer function [4].

Atomic emission spectroelectrochemistry (AESEC) provides a direct measurement of elemental dissolution rates [5]. One of the difficulties of this technique is that dissolution may be directly related to a faradaic process, weakly related as in the case of anodic dissolution by way of an oxide intermediate, or unrelated as when dissolution is due to a non-faradaic process. The correlation of electrochemical current transients with dissolution transients is one means of distinguishing between these possibilities as demonstrated by Jiang *et al*. [6, 7] for the dissolution of Zn in the presence of conversion coatings. The coupling of EIS and AESEC allows for a more sophisticated analysis of dissolution kinetics: the oscillating elemental dissolution rates may be related to the oscillating current and the EIS data may be decomposed into elemental components at least for the low frequencies. In this way, the EIS measurement may be obtained on an element

by element basis with the advantage that dynamic systems may be treated directly, by analyzing data in the time domain. A detailed model for AESEC-EIS was developed by Shkirskiy and Ogle [8], directly correlating the elemental dissolution rate and electrical current for pure Zn at open circuit potential. Zn dissolution in 0.1 M NH_4Cl occurred without any significant intermediate film formation as evidenced by the Zn dissolution rate being in-phase with the alternating current (AC) component of the electrical current. In 0.5 M NaCl solution, no correlation between the AC and the Zn dissolution rate was observed, indicating that oxide film formation and dissolution were decoupled faradaic and non-faradaic processes, respectively. The goal of this article is to extend the previous work to a multi-element system and to use the EIS spectra to distinguish different mechanisms of dissolution by taking advantage of the time-resolved measurement of each element of a multi-element system that AESEC technique provides.

The Al-Zn alloy system in alkaline solution was considered an ideal system for an early demonstration of the method. The system is industrially significant: Al-Zn alloys are commonly used as galvanic coatings on steel and occur as separate phases in Zn containing Al alloys, such as the 6000 series, and are almost always exposed to alkaline solution in their lifetime either during surface treatment by alkaline etching, or during corrosion when the cathodic reaction leads to local pH changes. The mechanisms of anodic and cathodic dissolution of multi-phase Zn-5 wt.% Al alloy coatings on steel were previously investigated [9, 10]. A complex interaction between the Zn and Al was observed, however, interpretation of the mechanisms of these interactions was hindered due to the multi-phase nature of the commercial coating material. Therefore, to simplify, we isolated the chemistry of a single phase: the α-phase of Al-Zn (Zn-68 wt.% Al). The anodic dissolution of Al and Zn were investigated as a function of potential in slightly alkaline (pH =

10.1) [11] and alkaline (pH = 12.8) [12] electrolytes. In the latter, the temperature dependence of anodic dissolution was also investigated [13].

In summary of these results, three potential domains were identified where the dissolution of the material occurred by very different mechanisms. Based on the individual Zn and Al dissolution rate results and the electrochemical current, it was found that Al underwent a direct, potential independent dissolution mechanism in the cathodic potential domain by reacting with H_2O, and without the formation of a significant intermediate oxide film. Metallic Zn accumulated on the surface in a mechanism of cathodic dealloying. In the anodic domain, Zn was transformed into an oxide film and Al dissolution occurred by ionic transfer across the film. As the two mechanisms are very different, it was felt that EIS coupled to AESEC might further confirm these mechanisms and allow a higher degree of precision on the mechanistic details.

Results and discussions

Overview of $Al_{5.2}Zn$ mechanisms as a function of potential

The sensitivity of the Al-Zn dissolution mechanism to potential is evident from the AESEC-linear sweep voltammetry (AESEC-LSV) curve of $Al_{5.2}Zn$ (Zn-68 wt.% Al) phase in 0.1 M NaOH solution, shown in **Fig. 1**. Elemental dissolution rates (j_M) and the convoluted electrical current density (j_e^*) as a function of potential are given with 0.5 mV s^{-1} scan rate. As previously described, the polarization curve clearly shows three potential domains, to which can be ascribed three unique mechanisms of dissolution. The *cathodic dealloying domain* occurs between -1.72 V to -1.35 V vs. Hg/HgO. It is characterized by an intense Al dissolution rate, j_{Al}, and a Zn

dissolution rate, j_{Zn}, close to the detection limit. A direct reaction between Al and H_2O was inferred with significant hydrogen evolution reaction (HER) [14] and accumulation of metallic Zn.

$$AlZn_x + 4H_2O + e^- \rightarrow Al(OH)_4^- + xZn(s) + 2H_2(g) \quad [1]$$

Al dissolution rate was potential independent and in fact, did not reflect or correlate in anyway with the electrochemical current the magnitude of which was much lower and changed sign during this potential domain.

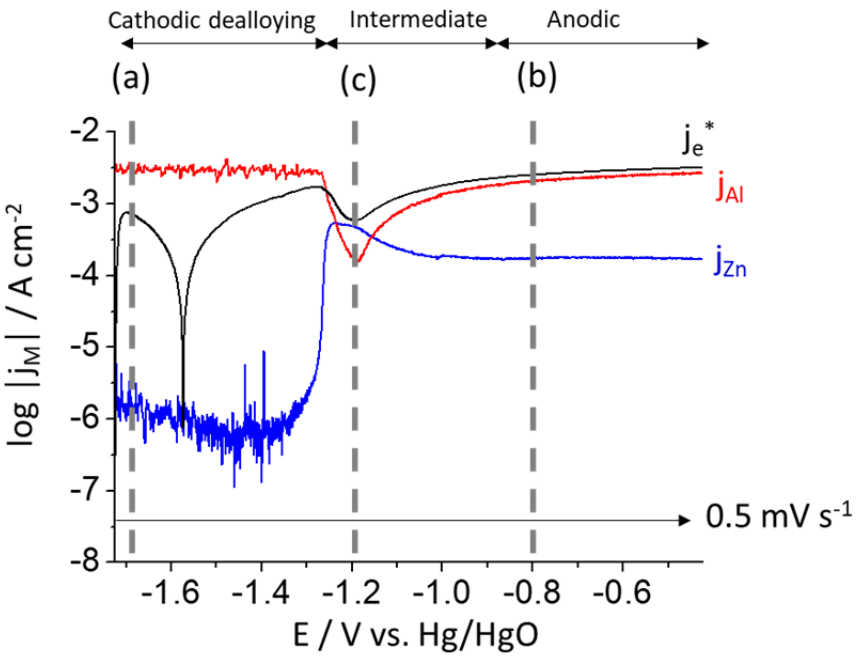

Fig. 1. *Elemental AESEC-LSV curve of $Al_{5.2}Zn$ phase in 0.1 M NaOH, pH=12.80, Ar deaerated electrolyte at T = 25°C. All potential values presented in this work are referenced to an Hg/HgO electrode in 0.1 M NaOH (-165 mV vs. SHE). Vertical dashed lines are selected potential values in the (a): cathodic dealloying, (b): anodic and (c): intermediate domains.*

A totally different mechanism is apparent in the *anodic domain* (from -0.9 V to -0.4 V vs. Hg/HgO), evidenced by the nearly congruent dissolution of Zn and Al, and the significantly decreased amplitude of perturbations in the j_{Al} signal. The DC faradaic yield of elemental dissolution may be determined as $\eta_{DC} = j_{\Sigma} / j_e^*$ when cathodic current contribution is negligible, where $j_{\Sigma} = j_{Zn} + j_{Al}$. In this case, the dissolution rate follows the electrical current with nearly a 100% DC faradaic yield ($\eta_{DC} = 0.98$) of dissolution. The potential independence of Zn and Al dissolution rates suggests an oxide film formation type of mechanism and indeed, Raman spectroscopy and SEM analysis also demonstrated the formation of ZnO layer in this potential domain [11, 12]

The elemental dissolution rates in the *intermediate domain* (from -1.35 V to -0.90 V vs. Hg/HgO), is more complex and involves the accumulated metallic Zn enriched layer, Zn(0), that was formed in the cathodic domain by the preferential Al dissolution. At the onset of Zn dissolution, there is a notable decrease in the j_{Al}, that we previously termed a *negative correlation effect* (NCE) in [12]. The j_{Zn} reached its maximum value in approximately the same potential domain as j_{Al} obtained its minimum value.

AESEC-EIS results

To corroborate and gain further insight into the proposed dissolution mechanisms, potentiostatic EIS was performed simultaneously with AESEC in the three potential domains, at potentials indicated as (a), (b), and (c) in **Fig. 1**. The Nyquist plots are presented in **Fig. 2** and the corresponding AESEC-EIS dissolution profiles are given in **Figs.** 3A – 3C. The effective oxide

capacitance (C_δ) values determined by the complex capacitance curve [15], the constant phase element (CPE) parameters (α and Q), and the corresponding effective oxide layer thicknesses (δ) for each potential domain are summarized in **Table 1**.

The Cathodic Dealloying Domain (-1.72 V to -1.35 V vs. Hg/HgO)

EIS in the cathodic dealloying domain (**Fig. 2A**) revealed a single time constant suggesting that H_2O reduction reaction was the dominating charge transfer reaction. The dissolution profile obtained by AESEC (**Fig. 3A**) again demonstrates the potential independence of Al dissolution, as the potential cycles at low frequency do not appear as oscillations in the elemental dissolution rates. This is an important conclusion because it indicates that the EIS spectra are revealing information on the interfacial electrochemical processes that may not directly affect the dissolution rate.

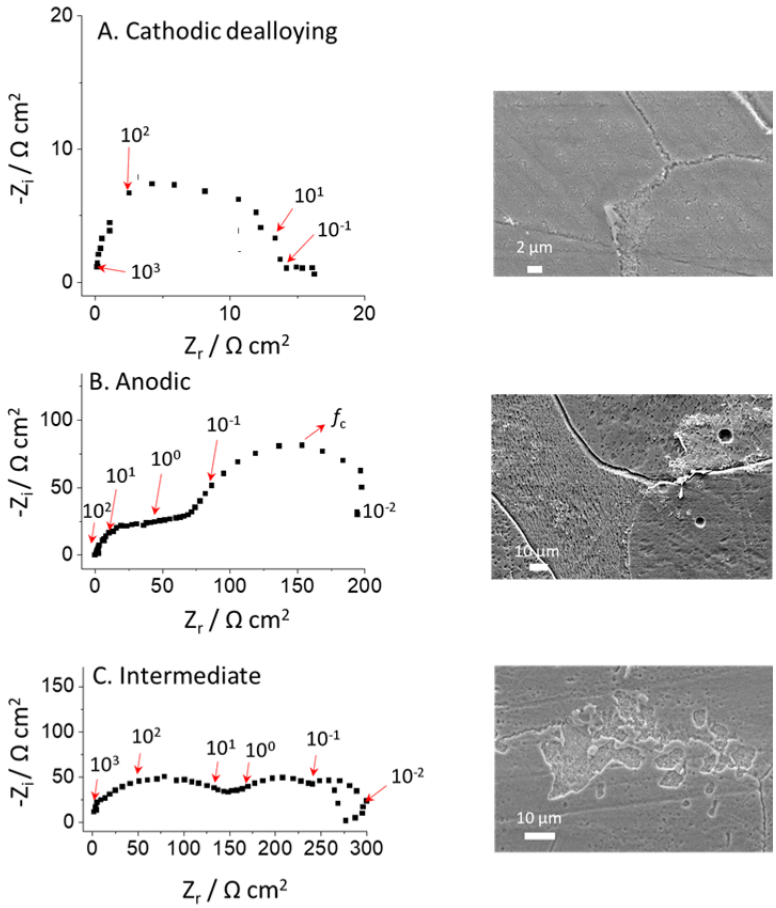

135

136 ***Fig. 2.*** *Nyquist plots at each potential domain determined from* ***Fig. 1*** *and their corresponding*

137 *SEM images; A: -1.70 V vs. Hg/HgO, B: -0.80 V vs. Hg/HgO and C: -1.20 V vs. Hg/HgO. Arrows*

138 *are indicating frequency values (Hz).*

139

140

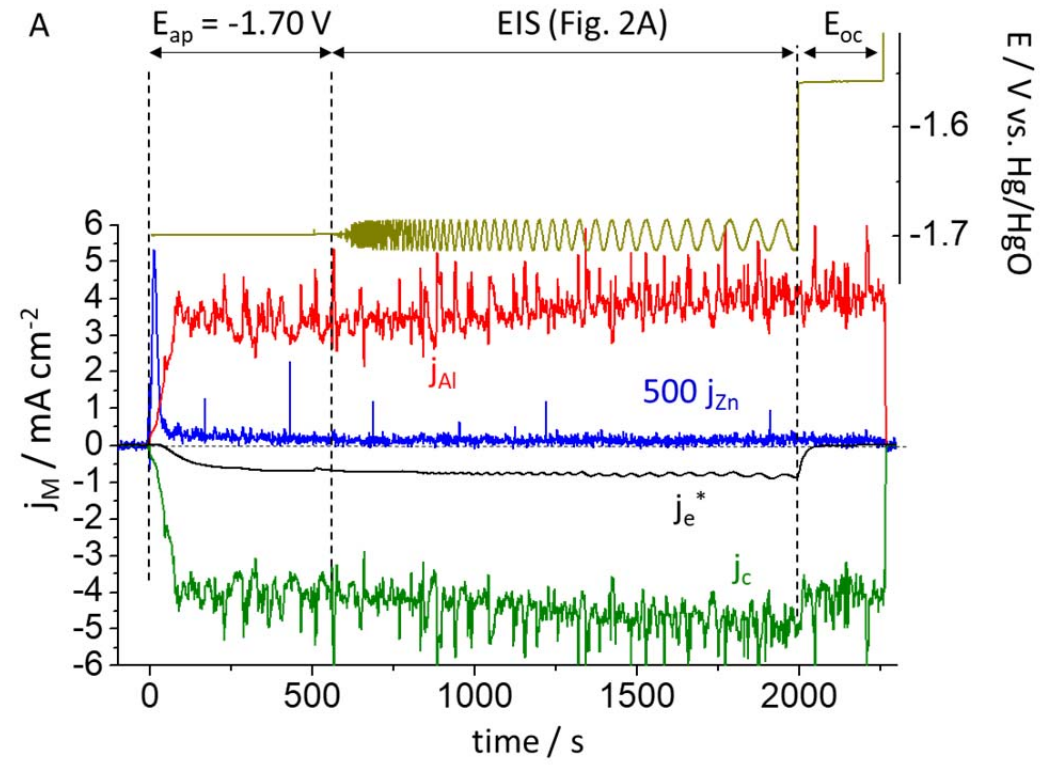
A
E_ap = -1.70 V
EIS (Fig. 2A)
E_oc
E / V vs. Hg/HgO
-1.6
-1.7
j_M / mA cm^-2
j_Al
500 j_Zn
j_e*
j_c
time / s

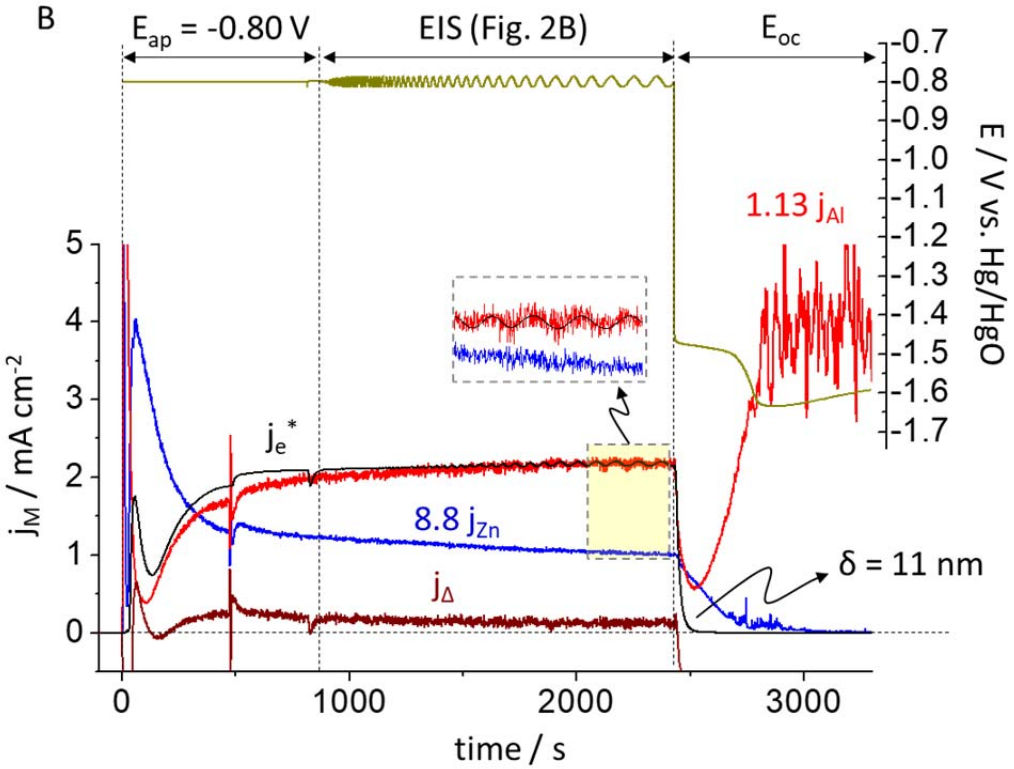
B
E_ap = -0.80 V
EIS (Fig. 2B)
E_oc
E / V vs. Hg/HgO
1.13 j_Al
j_M / mA cm^-2
j_e*
8.8 j_Zn
j_Δ
δ = 11 nm
time / s

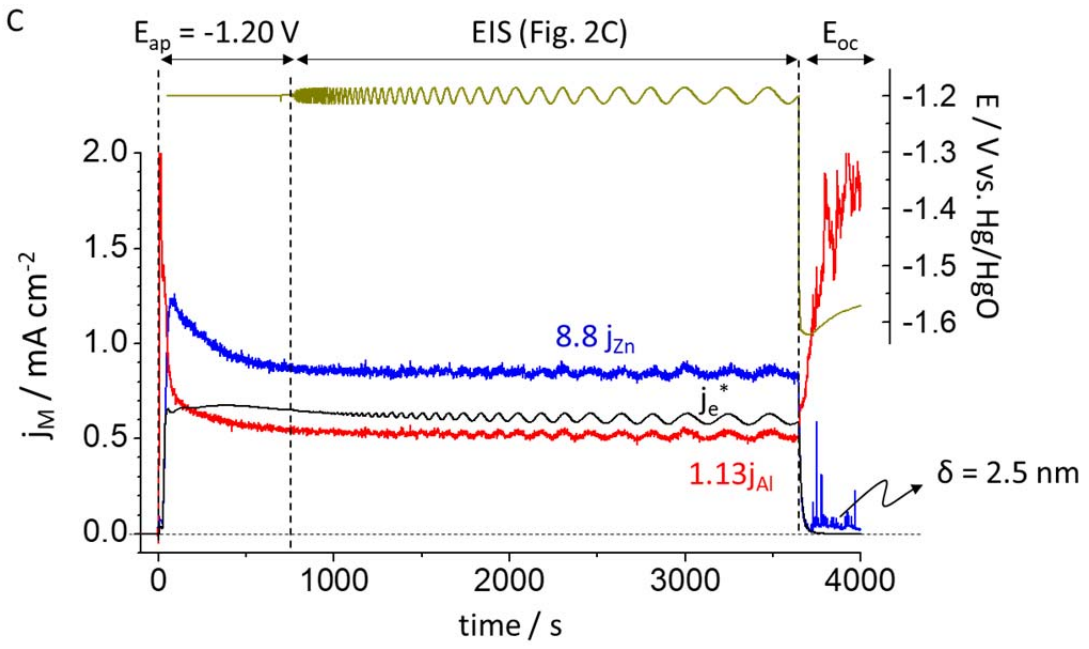

Fig. 3. *AESEC-EIS curve of $Al_{5.2}Zn$ in 0.1 M NaOH, Ar deaerated electrolyte including potentiostatic hold (E_{ap}), EIS and open circuit measurement (E_{oc}). **A**: E_{ap} = -1.70 V vs. Hg/HgO, **B**: E_{ap} = -0.80 V vs. Hg/HgO and **C**: E_{ap} = -1.20 V vs. Hg/HgO. j_M (M = Zn or Al) values are normalized based on the molar composition for **B** and **C**.*

141

142 The analysis of the high frequency loop shows a CPE behavior where $\alpha = 0.73$ and $Q = (1.07 \pm 0.20) \times 10^{-3}\ \Omega^{-1}\ cm^{-2}\ s^{\alpha-1}$, estimated from a graphical analysis [16]. Assuming that this
144 time constant is attributed to a 2D frequency distribution [17], Brug's relationships [18] allow an
145 estimation of the equivalent capacitance from the CPE parameters, in this case the double layer
146 capacitance, $C_{dl} = 191\ \mu F\ cm^{-2}$. This value is about an order of magnitude larger than the
147 expected value for a double layer capacitance and could represent the response of a very thin,
148 perhaps a non-uniform oxide film. It is reasonable to suppose that $Al(OH)_3$ forms as a short lived

intermediate in Reaction 1 as previously discussed [12, 13]. Reaction 1 may be broken down into more elementary steps as follows:

$$3H_2O + 3e^- \rightarrow 3/2\ H_2 + 3OH^- \quad [2]$$

$$AlZn_x + 3OH^- \rightarrow Al(OH)_3 + xZn\ (s) + 3e^- \quad [3]$$

$$Al(OH)_3 + OH^- \rightarrow Al(OH)_4^- \quad [4]$$

AESEC directly measures Reaction 4, which involves no electron transfer and in principle should be potential independent. The EIS results indicate that water reduction was potential dependent (**Fig. 2A**). This confirms the conclusions of [13]; the dissolution of Al oxide/hydroxide layer (Reaction 4) was the rate determining step (RDS) in accordance with previous studies [19, 20, 21, 22]. At steady state, Reactions 3 – 4 must occur at identical rates. The properties of the film most likely determine the reaction rate by controlling the access of H_2O to Al metal. The presence of the film may not be directly detected by AESEC due to the intense dissolution rate and cathodic current, however, the film is detected indirectly by EIS. The cathodic current resulting from the HER may be determined simply as $j_\Delta = j_e^* - j_\Sigma = j_c$, shown in **Fig. 3A**.

The anodic domain (-0.9 V to -0.4 V vs. Hg/HgO)

In the anodic domain, the polarization curve (**Fig. 1**) demonstrates that Zn and Al dissolution rates and the electrochemical current are stable and nearly independent of potential. In the EIS spectrum (**Fig. 2B**), three-time constants are observed. The high frequency capacitive loop may be attributed to the charge transfer resistance of Zn and / or Al oxidation in parallel with the interfacial capacitance. In this system, independent anodic dissolutions from Zn and Al

simultaneously occur at different rate and thus the admittance is the sum of these contributions. This may explain why the two entangled time constants are observed in the high frequency domain. The low frequency loop shows a nearly 45° phase that suggests a diffusion process [23, 24]. The time constant observed at intermediate frequency (approximately f = 1 Hz) is poorly resolved due to overlap with the high and low frequency contributions and will not be discussed.

The high frequency capacitive loop is flattened and this can be described by a CPE in parallel with the charge transfer resistance. We assume that this CPE is due to the distribution of properties in a thin oxide film [16], for instance, the distribution of resistivity according to a power-law model [25, 26]. From the analysis of the complex capacitance calculated from the impedance data [15], the high frequency limit of the of the capacitance was $C_\delta = 0.65 \pm 0.05$ μF cm^{-2}. Such a low value is characteristic of the dielectric response of a thin oxide film. Assuming a dielectric constant $\varepsilon = 8.8 \pm 0.8$ for ZnO [27] the thickness of the thin oxide film, δ, formed at the electrode interface is given by;

$$\delta = \varepsilon \, \varepsilon_0 / C_\delta \qquad [5]$$

where ε_0 is the vacuum permittivity (8.85×10^{-14} F cm^{-1}). This equation yields $\delta = 12 \pm 1$ nm. Such a value confirms the hypothesis that the interfacial capacitance is governed by the thin oxide film contribution (*i.e*. the double layer capacitance which is in series with the capacitive contribution of the oxide film, has in this case a negligible contribution).

The presence and characteristics of the oxide film may be further refined by consideration of the low frequency capacitive loop. For the AESEC-EIS (**Fig. 3B**), very slight oscillations are observed in the Zn and Al dissolution rate at low frequency (magnified curve is given in the

inset). The faradaic yield of dissolution for the total current, η_{DC} = 0.96 ± 0.03 close to 1, in agreement with [12]. The faradaic yield of the AC component, η_{AC}, is defined as:

$$\eta_{AC} = \text{AC amplitude } (j_{\Sigma}) \text{ / AC amplitude } (j_e^*) \qquad [6]$$

From the data in **Fig. 3B**, η_{AC} = 1.01 ± 0.05, reasonably identical to η_{DC} within experimental error. Note that error bar of η_{AC} was obtained from different frequency domains. It appears to be distributed essentially in the Al dissolution although slight peaks above background are observed for Zn dissolution as well.

The second capacitive loop in **Fig. 2B** shows a typical diffusion-controlled charge transfer mechanism through an oxide layer [24]. Interestingly, the characteristic frequency, $f_{c,}$ = 0.032 Hz at the apex of the time constant of the diffusion process in the Nernst layer may be expressed as;

$$f_c = 2.51\ D / 2\pi\ \delta^2 \qquad [7]$$

where δ is the thickness of the corrosion product, that can be in a first approximation evaluated to be at least the thickness previously obtained from the CPE parameter (δ = 12 nm). The diffusion coefficient may be calculated from **Eq. 7**, D = 1.15 x 10^{-13} cm^2 s^{-1}. Such a low value should be due to the underestimated δ value because the calculation did not consider the porosity of the oxide as well as the accumulation of corrosion products at the electrode surface. It may be attributed to a diffusion of species inside of a micrometric diffusion layer of corrosion product. In this case, the diffusion and migration caused by the large electric filed inside the film should be taken into account.

A. E_{ap} = -0.80 V vs. Hg/HgO

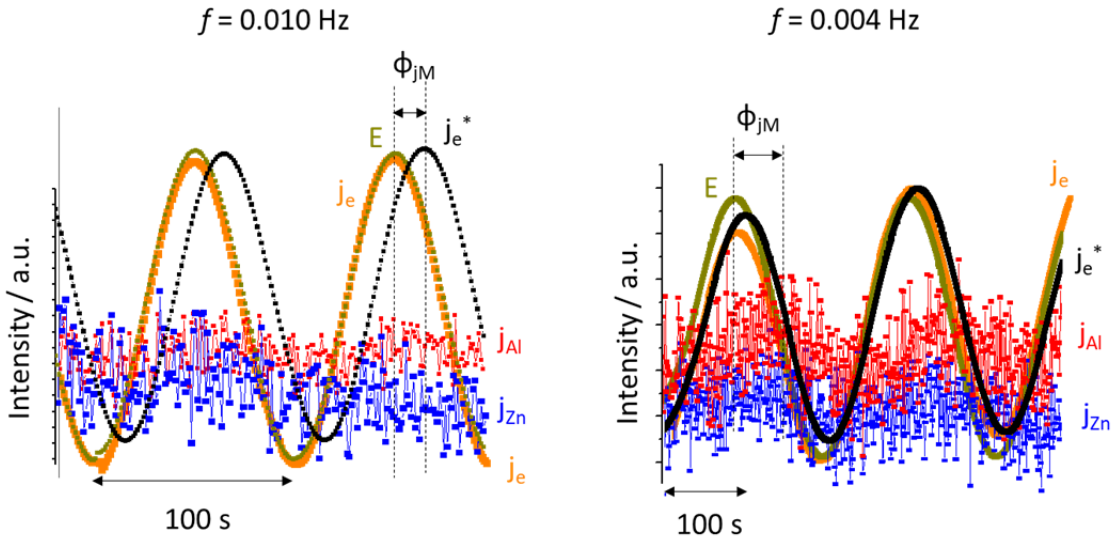

B. E_{ap} = -1.20 V vs. Hg/HgO

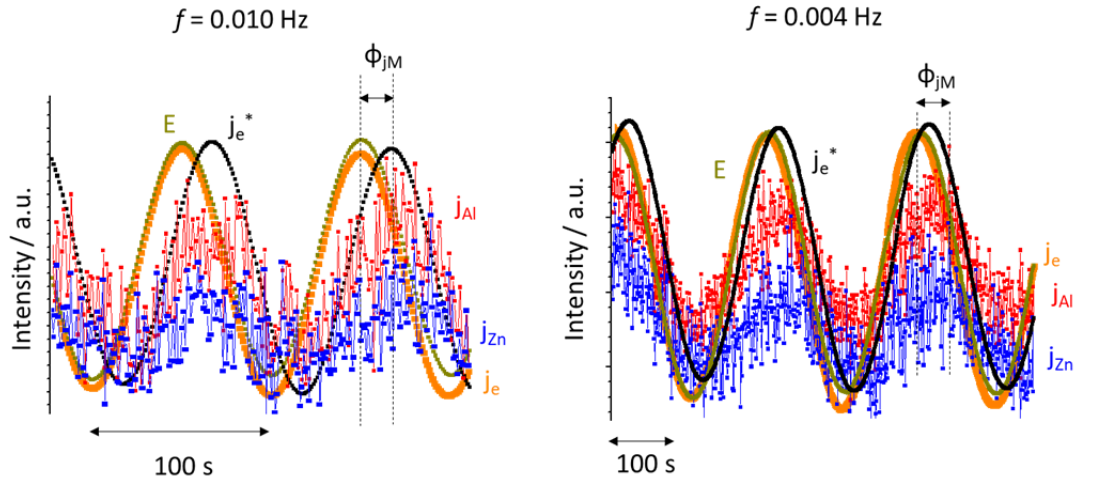

Fig. 4. *The oscillation trends at low frequency domain for A: E_{ap} = -0.80 V vs. Hg/HgO and B: E_{ap} = -1.20 V vs. Hg/HgO from Figs. 3B and 3C, respectively.*

211

212 **Fig. 4** shows the oscillation trends of the j_e, j_e^*, j_M and applied potential (E) at a given

213 frequency of AESEC-EIS result from **Fig. 3**. To facilitate the comparison, each profile is

presented in arbitrary units. The phase shift of j_M and j_e^* vs. E (ϕ_{j_M}) results from the residence time distribution of the flow cell [5], which means that it is not frequency dependent but time dependent. The actual phase shift between E and j_e (ϕ) was nearly zero in all cases as shown in **Fig. 4**.

The impedance contribution from each elemental dissolution in real part, Z_r (j_M), is given in **Table 2**, calculated at each frequency domain as:

$$Z_r (j_M) = (|d E| / |d j_M|) \cos(\phi) \quad [8]$$

For E_{ap} = -0.80 V vs. Hg/HgO (**Fig. 4A**), j_{Zn} oscillation is less evident than at E_{ap} = -1.20 V vs. Hg/HgO (**Fig. 4B**), probably indicating a weak potential dependent Zn dissolution in the anodic potential domain due to the Zn-based corrosion products formation. The high Z_r (j_{Zn}) values at E_{ap} = -0.80 V vs. Hg/HgO could also be explained by the weak potential dependency of Zn dissolution at this potential. For E_{ap} = -1.20 V vs. Hg/HgO, Z_r (j_{Zn}) + Z_r (j_{Al}) ≈ $Z_r - R_e$, which may indicate that j_{Zn} and j_{Al} contributed to the total impedance with a parallel relationship. Note that Z_r is measured by potentiostat then subtracted by the electrolyte impedance, $Z_e = R_e$. It is consistent with the previously proposed dissolution model of the $Al_{5.2}Zn$ phase in which Al dissolution occurred through a porous Zn(0) layer in parallel with Zn dissolution [12]. It should be mentioned that the dissolution is not a simple mechanism as it usually involves the adsorbed intermediate species which may result in a delay between the j_e^* and j_M.

The correlation between the AC current and dissolution rates is highlighted by the Lissajous analysis in **Figs. 5A** (E_{ap} = -0.80 V vs. Hg/HgO) and **5B** (E_{ap} = -1.20 V vs. Hg/HgO) at f = 0.004 Hz. j_e^* curve is shown on the top, both for upper and lower potential scans. For j_M vs. E

curves in the middle, j_e^* assuming congruent dissolution of Al and Zn are also shown. For example in **Fig. 5A**, Al dissolution was congruent as $j_{Al} \approx (j_e^* / 1.13)$ whereas Zn dissolution was not as $j_{Zn} < (j_e^* / 8.8)$. The correlation of Zn dissolution rate with potential is less obvious than for Al, but exists (also see **Fig. 4A**). In principle, at this potential, there is no significant cathodic reaction, so we conclude that the AC current is primarily going to the formation and reduction of ZnO or $Zn(OH)_2$. It was previously shown that the $\eta_{AC} \approx \eta_{DC} \approx 1$ at E_{ap} = -0.80 V vs. Hg/HgO, supporting this assumption. The weak correlation is interesting since the overall faradaic yield of dissolution based on the DC current density and elemental dissolution rates was nearly 100% ($\eta_{DC} = 0.96 \pm 0.03$) at this potential. In this case, it could be concluded that the DC component was due to the dissolution of the corrosion products [6, 7, 28].

255

A. E_{ap}=-0.80 V vs. Hg/HgO (0.004 Hz)

B. E_{ap}=-1.20 V vs. Hg/HgO (0.004 Hz)

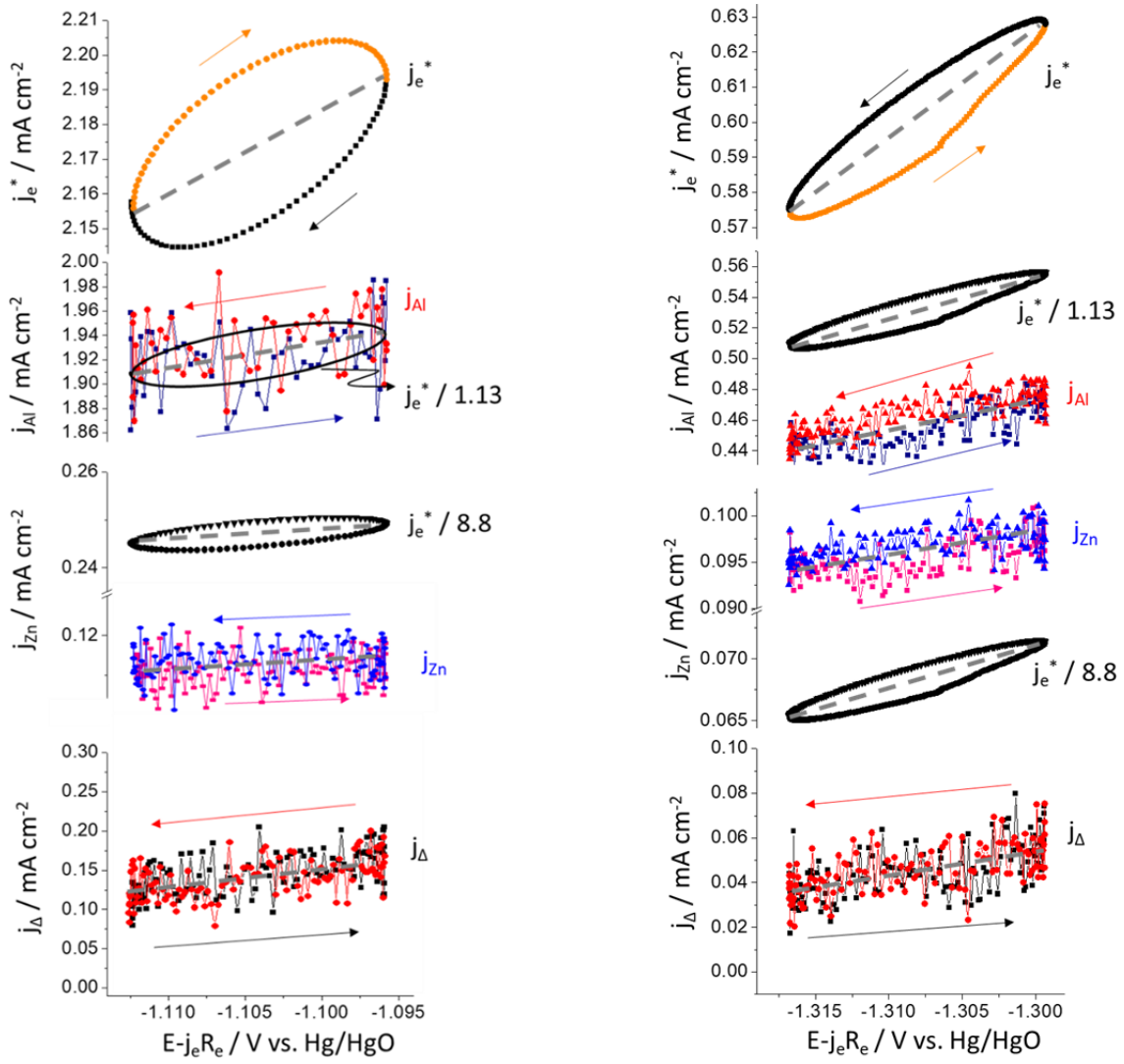

Fig. 5. *Lissajous analysis at f = 0.004 Hz at* ***A****:* E_{ap} *= -0.80 V vs. Hg/HgO and* ***B****:* E_{ap} *= -1.20 V vs. HgO. The* j_e^*, j_{Al} *and* j_{Zn} *are shown as a function of IR drop compensated applied potential (E-*j_eR_e*). One cycle including upper and lower potential scans, indicated by arrows, is given.*

256

The kinetic parameters for ZnO formation and reduction may be estimated from the j_Δ vs. E Lissajous plot, shown in the bottom of **Fig. 5**. The Zn dissolution in the anodic potential domain (**Fig. 5A**) may be the combination of a series of elementary reactions as:

$$Zn + 2OH^- \rightarrow Zn(OH)_2 + 2e^- \ (j_\Delta) \qquad [9]$$

$$Zn(OH)_2 + OH^- \rightarrow Zn(OH)_3^- \qquad [10]$$

$$Zn + Zn(OH)_2 + 2OH^- \rightarrow 2ZnO + 2H_2O + 2e^- \ (j_\Delta) \qquad [11]$$

$$ZnO + OH^- + H_2O \rightarrow Zn(OH)_3^- \ (j_{Zn}) \qquad [12]$$

The intermediate species such as ZnOH or $ZnOH_{ads}$ [29, 30, 31] are not considered as the time scale of the AESEC experiment is too slow to measure these species. The formation rate of $Zn(OH)_2$ or ZnO (j_Δ) is potential dependent (Reactions 9 and 11) given that the Lissajous plot of j_Δ vs. E showed the linearity, neglecting the contribution of cathodic current at this potential. The anodic Tafel slope of j_M ($b_{a,\, j_M}$) may be calculated as;

$$b_{a,\, j_M} = 2.303 \ \Delta E \ / \ \ln(j_M^+ / j_M^-) \qquad [13]$$

where j_M^+ and j_M^- are j_M values measured at the highest and lowest potential, respectively. ΔE is the difference between the highest and lowest potential. $b_{a,\, j_\Delta} = 94$ mV decade^{-1} and $b_{a,\, j_{Zn}} = 2350$ mV decade^{-1} are calculated by Eq. 13. It is clearly demonstrated that the formation of ZnO (Reaction 11) is faster than the dissolution (Reaction 12), resulting in the growth of the ZnO layer [12, 13].

The quantity of oxide formed during the AESEC-EIS experiment may be estimated by the dissolution profile obtained after releasing the potential to open circuit at the end of the experiment. The E_{ap} = -0.80 V vs. Hg/HgO AESEC-EIS profile of **Fig. 3B** illustrates this idea. At the end of the experiment, the presence of oxide dissolution is indicated by a plateau in the E_{oc} vs. time profile at approximately E_{oc} = -1.50 V vs. Hg/HgO. The removal of the oxide and the exposure of the underlying metallic substrate is indicated by the sudden drop in potential to < -1.6 V vs. Hg/HgO. The removal of the oxide film gives rise to a transient dissolution of Zn, which decays steadily but at a rate significantly slower than the residence time distribution associated with the flow cell. The latter is indicated by the drop of the convoluted electrochemical current, j_e^*. Integration of the j_{Zn} yields a thickness of ZnO layer δ = 11 nm was obtained assuming a uniform ZnO layer formation over the geometrical surface area and a ZnO density of 5.6 g cm^{-3}. This is in the same range as the thickness estimated from EIS of 12 ± 1 nm (**Table 1**).

The Intermediate Domain (-1.35 V to -0.9 V vs. Hg/HgO)

In the intermediate domain, both j_{Zn} and j_{Al} showed clear in-phase oscillations, with the low frequency AC current (**Fig. 3C**). The EIS response in **Fig. 2C** shows three capacitive time constants and one inductive loop. An inductive loop has already been reported for both Zn and Al dissolution. In the case of Zn, this loop is usually observed in the intermediate frequency range [24, 32] whereas for Al, it can be only be seen in the low frequency domain in an alkaline solution [33, 34]. We thus conclude that the inductive loop observed for $f < 10^{-2}$ Hz may be attributed to the relaxation of the surface intermediates involved in the dissolution mechanism of

297 Al and Zn [35]. The third capacitive loop is similar to the one observed at E_{ap} = -0.80 V vs.
298 Hg/HgO and may be ascribed to diffusion processes inside a thin layer. The characteristic
299 frequency is also similar to the previous case in **Fig. 2B** confirming that convection-diffusion
300 controlled mechanism by the flux of the electrolyte in the AESEC experiment.

301 The second capacitive loop (10^{-1} Hz < f < 10^{0} Hz) was also distributed and its analysis is
302 complicated by the fact that it is convoluted with other processes at both higher and lower
303 frequency. However, it may be ascribed to Zn dissolution [24]. The high frequency time constant
304 was analyzed as previously described. From the CPE behavior, the oxide film thickness was
305 estimated at δ = 2.4 nm. The analysis of the high frequency loop for each potential showed that
306 the thin film formed on the alloy surface has a thickness that strongly depends on the applied
307 potential.

308 In **Fig. 3C**, a peak of Zn dissolution is observed after the potential release, albeit a much
309 smaller peak than at E_{ap} = -0.80 V vs. Hg/HgO (**Fig. 3B**). Nevertheless, this peak cannot be
310 unequivocally attributed to oxide dissolution as there is no clearly defined potential plateau
311 following the potential release. Assuming that this peak was due to oxide dissolution, an
312 estimated thickness of 2.5 nm is obtained with the same assumptions as before, in good
313 agreement with that obtained from the EIS analysis of 2.4 ± 0.3 nm (**Table 1**).

314 The low frequency Lissajous plots at E_{ap}=-1.20 V vs. Hg/HgO (**Fig. 5B**) show linear
315 behavior within experimental error indicating that the elemental dissolution current (j_M) for each
316 species is in-phase with the potential. In this case, the linearity of the Lissajous plots of j_{Zn} and j_{Δ}
317 is clearly demonstrated, indicating that both reactions are charge transfer limited. The cathodic
318 current would make a negligible contribution to j_e^* as E_{ap} was approximately +400 mV than the

zero current potential ($E_{j=0}$). The Zn oxidation reaction may be written by the combination of Reactions 9 and 10 as;

$$Zn + 3OH^- \rightarrow Zn(OH)_3^- + 2e^- (j_{Zn}) \quad [14]$$

and the formation of the ZnO (j_Δ) is via Reaction 11. $b_{a,\, j_\Delta}$ = 68 mV decade^{-1} and $b_{a,\, j_{Zn}}$ = 864 mV decade^{-1} were obtained by Eq. 13 from **Fig. 5B**. Given that the Tafel slope of j_{Zn} at E_{ap} = -1.20 V vs. Hg/HgO is lower than that at E_{ap} = -0.80 V vs. Hg/HgO, it could be concluded that the dissolution of Zn is faster in former case resulting in a relatively thinner ZnO layer formation.

In this case, both Zn and Al dissolution were not faradaic in that $j_e^* / 1.13 \neq j_{Al}$ and $j_e^* / 8.8 \neq j_{Zn}$ (**Fig. 5B**). It showed a significant difference between η_{DC} = 0.92 ± 0.02 and η_{AC} = 0.65 ± 0.03. It was proposed that the AC component is due to non-faradaic reactions at the metal/oxide interface and the DC component to the faradaic dissolution of the film at the oxide/electrolyte interface [6, 7, 28]. For the AC case in the intermediate domain, it can be concluded that formation of the corrosion product would be the RDS, given that $\eta_{DC} >> \eta_{AC}$, consistent with the Tafel slope analysis. A simplified elemental dissolution at each interface in anodic potential domain is illustrated in **Fig. 6**. The system extends our previous work with AESEC-EIS in that the potential dependent and potential independent mechanisms are observed for two different elements of a single system. In the previous work they were observed for Zn in different electrolytes [8].

Interestingly, j_{Zn} was higher than its congruent dissolution level ($j_e^* / 8.8$) whereas j_{Al} was lower than $j_e^* / 1.13$. The excess Zn dissolution could lead to a restrained Al dissolution, referenced as the *NCE* [12].

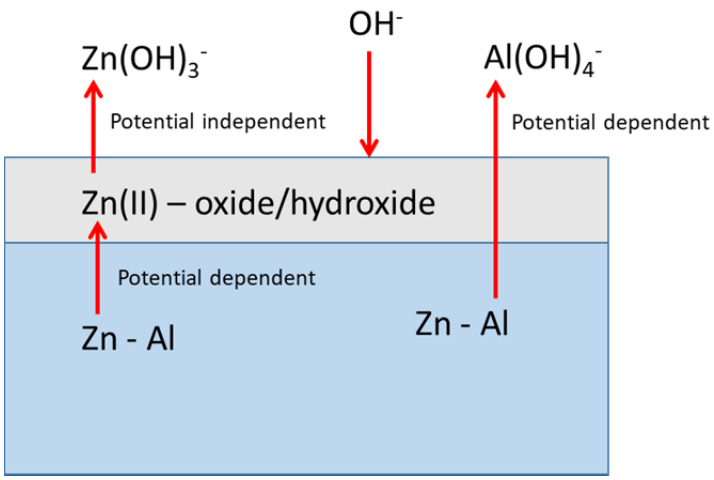

Fig. 6. *Simplified schematic model of elemental dissolution at each interface of* Al_xZn *in 0.1 M NaOH solution in anodic potential domain.*

340

341 **$Al_{0.7}Zn$ (Zn-22 wt.% Al)**

342 In this section, we will demonstrate the AESEC-EIS methodology with a system that is
343 intrinsically unstable and shows a more usually observed dissolution case for the lower Al
344 content Zn-Al system [36]. An AESEC-EIS curve (**Fig. 7A**), magnified oscillation trends at f =
345 0.010 Hz (**Fig. 7B**) and a corresponding Nyquist plot (**Fig. 7C**) for the $Al_{0.7}Zn$ (Zn-22 wt.% Al)
346 nominally pure phase at E_{ap} = -1.36 V vs. Hg/HgO (*i.e.* +150 mV from $E_{j=0}$) in the same
347 electrolyte are given. It is clear from Fig. 7A that the elemental dissolution mechanism varies
348 throughout the time period of the experiment. Initially, Zn dissolution was intense at
349 approximately the same level as Al. However, for t > 2700 s (f < 0.005 Hz), j_{Zn} decreased to
350 under the detection limit and Al dissolution changed from a charge transfer to a chemical
351 dissolution mechanism. The latter is indicated by the disappearing oscillation of j_{Al}, and the
352 significantly increased j_{Al} noise signal indicating HER [12, 14]. The non-charge transfer Al

dissolution mechanism is also revealed in the Nyquist plot (Fig. 7C) where an unambiguous diffusive impedance trend was observed ($\phi = 45^{\circ}$) in this frequency domain. $ZnO/Zn(OH)_2$ formation and dissolution would occur for $f \geq 0.007$ Hz as Reactions 9 - 12:

A.

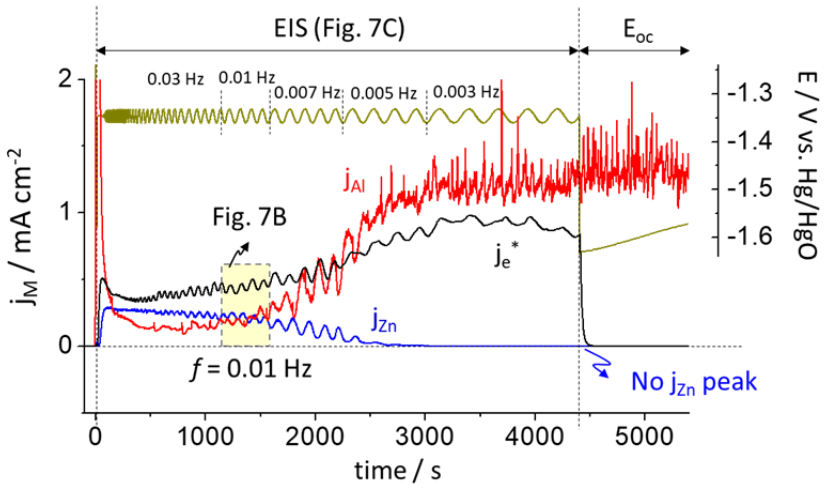

B.

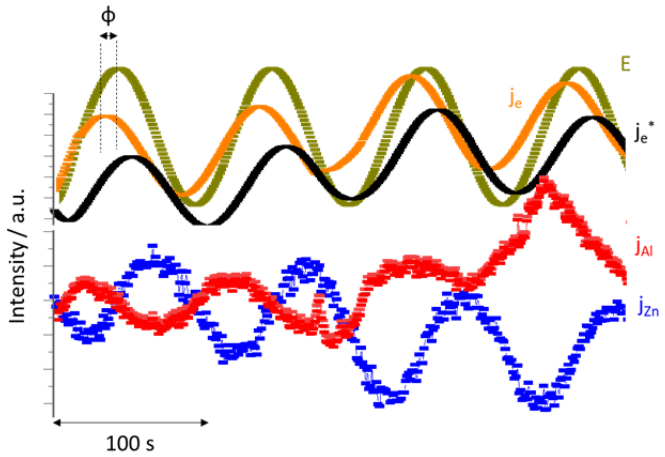

C.

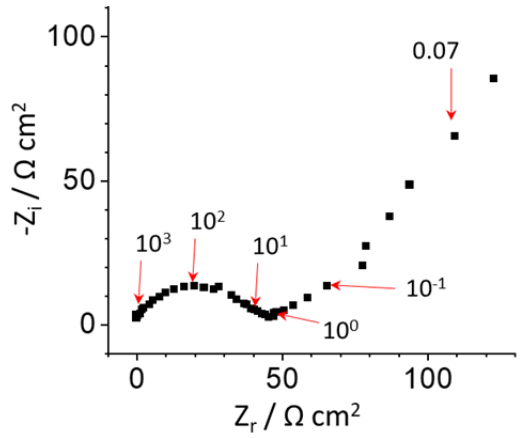

***Fig. 7. A**: AESEC-EIS curve of Zn-22 wt.% Al in 0.1 M NaOH, Ar deaerated electrolyte, at E_{ap} = -1.36 V vs. Hg/HgO, **B**:* oscillation trends at *f* = 0.010 Hz, and ***C**: corresponding Nyquist plot*.

j_{Zn} showed a clear oscillation from a relatively higher frequency domain ($f \approx 0.030$ Hz) where no j_{Al} oscillation was observed. j_{Al} oscillation disappeared with the dissolution of $ZnO/Zn(OH)_2$ for t > 2700 s, indicating that Al dissolution occurred through this Zn-based corrosion product layer (see also Fig. 6). The phase shift of E vs. j_e (ϕ) was not zero as summarized in **Table 3**, whereas $\phi \approx 0$ for $Al_{5.2}Zn$ (Fig. 4). The measured total impedance was close to the sum of each elemental contribution calculated from Eq. 8, $Z_r - Z_e \approx Z_r(j_{Zn}) + Z_r(j_{Al})$, similar to the $Al_{5.2}Zn$ in the same potential domain, which can be an indicative of the parallel relationship between Zn and Al dissolution. The phase shift between j_{Zn} and j_{Al} was 180˚ (**Fig. 7B**) whereas in-phase relation was monitored for $Al_{5.2}Zn$ (**Fig. 4**). The out-of-phase of j_{Zn} and j_{Al} should have been explained by the fact that Al dissolution is related to the cathodic reaction at open circuit potential [28]. However, it is not probable in the present work because this phase shift was observed at a relatively positive potential where cathodic current contribution is

negligible. One possible explanation is that in this potential domain, the slope of the Al dissolution rate - potential curve is negative [36] resulting in a negative low frequency-impedance [37, 38].

For $f \leq 0.007$ Hz, j_{Zn} decreased to under the detection limit as all the previously formed $ZnO/Zn(OH)_2$ dissolves. Previously for $Al_{5.2}Zn$ phase, a clear Zn dissolution peak was observed during the spontaneous dissolution after the AESEC-EIS experiments in **Figs. 3B and 3C**. It was attributed to the residual $ZnO/Zn(OH)_2$ dissolution formed during the potentiostatic experiment. In **Fig. 7**, no j_{Zn} peak was monitored in E_{oc} indicating that the oxide was completely dissolved near t = 2700 s.

Conclusion

In this work, we have demonstrated the application of combined AESEC-EIS to identify and quantify different anodic dissolution processes for a multi-element system, Al-Zn pure phase in 0.1 M NaOH. The elemental dissolution mechanism at each potential domain was elucidated by the AESEC-EIS technique.

AESEC gave immediate information on the elemental dissolution rates and transient behavior while EIS gave information on the physical properties of intermediate oxide layers and kinetic information for water reduction in the cathodic domain. A potential independent Al dissolution without forming an oxide layer was observed by AESEC-EIS at a cathodic potential domain (E_{ap} = -1.70 V vs. Hg/HgO).

By comparing the DC and AC faradaic yield, information on the localization of charge transfer reactions could be obtained. In the anodic domain (E_{ap} = -0.80 V vs. Hg/HgO), $\eta_{DC} \approx \eta_{AC}$ indicating that the formation and dissolution of the corrosion products occur at the nearly same rate, consistent with the previous observation [12, 13]. In the intermediate domain (E_{ap} = -1.20 V vs. Hg/HgO), formation would be the RDS as $\eta_{DC} >> \eta_{AC}$. In the former case, the oxidation of metal occurred through a corrosion product layer. In the latter case, the oxidation would occur directly from the metal/oxide complex. It was further demonstrated by the Tafel slope of j_{Zn} from the elemental Lissajous analysis (**Fig. 5**). In this way, AESEC-EIS can be utilized to distinguish the different elemental dissolution kinetics. Diffusion processes were identified although the precise origin was not ascertained, *i*. *e*. across corrosion product films or within inter-granular crevices and pits.

Elemental impedance contribution, Z_r (j_M), demonstrated the potential dependent elemental dissolution model of Al-Zn pure phase proposed in [12]. In the intermediate potential domain, Al dissolution occur through the porous Zn(0) enriched layer in parallel with Zn dissolution as Z_r (j_{Zn}) + Z_r (j_{Al}) ≈ total measured impedance ($Z_r - Z_e$).

For $Al_{5.2}Zn$, Al and Zn dissolution rates were in-phase regardless of the applied potential. For $Al_{0.7}Zn$ and other low Al content alloys and phases [36], Al and Zn dissolution rates showed a 180° phase shift. However, the origin of the phase shift is not ascertained to the satisfactory level.

Methods

410 *Materials*

411 A nominally pure phases of Al-Zn (Zn-68 wt.% Al and Zn-22 wt.% Al), provided and
412 characterized by the *Department of Metals and Corrosion Engineering, University of Chemistry*
413 *and Technology*, Prague, were investigated in this work. Zn-68 wt.% Al phase is denoted as
414 $Al_{5.2}Zn$ and Zn-22 wt.% Al as $Al_{0.7}Zn$, based on their molar compositions to facilitate the
415 congruent dissolution analysis. The chemical composition of these materials were 67.6 wt.% Al
416 and 32.4 wt.% Zn (Zn-68 wt.% Al), and 21.4 wt.% Al and 78.6 wt.% Zn (Zn-22 wt.% Al),
417 respectively, measured by atomic absorption spectroscopy (AAS). All samples were ground with
418 Si-C paper up to P4000 under ethanol, dried with flowing N_2 gas then stored in a humidity
419 chamber of 50% relative humidity with saturated $Mg(NO_3)_2 \cdot 6H_2O$ during 24 hours, providing a
420 reproducibly oxidized surface prior to the experiment [36, 39]. All the experiments were
421 performed in a 0.1 M NaOH (pH = 12.80) at T = 25°C, prepared from analytical grade materials
422 using deionized water obtained by a Millipore^{TM} system (18.2 MΩ cm). The electrolytes were
423 deaerated by Ar gas for 30 min prior to the tests and maintained during the experiments.

424

425 *Atomic emission spectroelectrochemistry (AESEC)*

426 The AESEC technique has been described in detail elsewhere [5, 40]. The working
427 electrode was in contact with the flowing electrolyte in a specially designed flow cell [5, 41] with
428 conventional three-electrode system; a Hg/HgO in 0.1 M NaOH (-165 mV vs. SHE) as a
429 reference electrode and a Pt foil as a counter electrode. The elements released from the working
430 electrode were transported to an Ultima 2C Horiba Jobin-Yvon inductively coupled plasma
431 atomic emission spectrometer (ICP-AES). The concentrations of Zn and Al were determined

from the emission intensity at 213.86 nm (Zn with a Paschen-Runge polychromator) and at 167.08 nm (Al with a monochromator) wavelength, respectively, using standard ICP-AES calibration techniques.

A Gamry Reference 600^{TM} potentiostat was used to perform electrochemical impedance spectroscopy (EIS) and linear sweep voltammetry (LSV). The electrochemical response (namely the electrical current density, j_e, and the electrode potential, E) were recorded in real-time with the elemental dissolution rates, using the analog data acquisition and the software interface (Quantum^{TM}, Horiba Jobin-Yvon) of the AESEC technique. The EIS was performed at different potentials from 100 kHz to 0.004 Hz with 8 points per decade of frequency and applying a 10 mV_{rms} sinewave perturbation.

Data analysis of the AESEC technique

The atomic emission intensity at a characteristic wavelength (λ) of the element M, $I_{M,\lambda}$, was recorded by the ICP-AES as a function of time downstream from an electrochemical flow cell. The elemental concentration (C_M) is calculated as;

$$C_M = (I_{M,\lambda} - I_{M,\lambda}^{\circ}) / \kappa_{\lambda} \qquad [15]$$

where $I_{M,\lambda}^{\circ}$ is the background signal, and is κ_{λ} the sensitivity factor of M, obtained from a standard ICP calibration method. The elemental dissolution rate (v_M) can be calculated from Eq. 15 with the flow rate of the electrolyte (f = 2.8 mL min^{-1}) and the exposed surface area A (1.0 cm^2) as:

$$v_M = f C_M / A \qquad [16]$$

453 The v_M was converted to an equivalent elemental current density (j_M) to facilitate comparison
454 with the electrical current density (j_e) measured by the potentiostat, in a relationship with;

455 $$j_M = z F v_M \quad [17]$$

456 where F is the Faraday constant and z is the valance of the dissolving species (Al^{3+}, Zn^{2+}). It is
457 often useful to present j_e^* which represents the measured j_e after a numerical convolution with the
458 residence time distribution in the flow cell (a lognormal distribution), thereby allowing a direct
459 comparison between the instantaneous values of j_e^* and j_M [5]. Cathodic reactions and the
460 formation of insoluble or slightly soluble species are not directly detected by ICP-AES. If surface
461 charging is neglected, the faradaic component of these hidden processes may be determined by a
462 mass-charge balance as:

463 $$j_\Delta = j_e^* - j_{Zn} - j_{Al} \quad [18]$$

464

465 *Surface characterization*

466 The sample surface after each potentiostatic AESEC-EIS experiment was characterized
467 by scanning electron microscopy (SEM) suing a Zeiss LEO 1530^{TM} microscope with field
468 emission gun source at 15 keV, and with 15 mm working distance. An equal mix of secondary
469 electron and back-scattered electron detector was used.

470

471 **Acknowledgement**

Authors would like to appreciate to Dr. Jan Stoulil, University of Chemistry and Technology in Prague, Czech Republic for supplying Zn-22 wt.% Al and Zn-68 wt.% Al samples.

Author Contributions

J. H. carried out the AESEC-EIS experiments and coordinated analysis between two techniques. V. V. was responsible for the EIS data interpretation. K. O. conceptualized the AESEC-EIS analysis. All authors contributed to write the paper and revision.

Data availability

The authors declare that the data supporting the findings of this study are available within the paper. The supplementary data will be available upon reasonable request.

Competing interests

The authors declare no competing interests.

Figure captions

Fig. 1. Elemental AESEC-LSV curve of $Al_{5.2}Zn$ phase in 0.1 M NaOH, pH=12.80, Ar deaerated electrolyte at T = 25°C. All potential values presented in this work are referenced to an Hg/HgO electrode in 0.1 M NaOH (-165 mV vs. SHE). Vertical dashed lines are selected potential values in the (a): cathodic dealloying, (b): anodic and (c): intermediate domains.

Fig. 2. Nyquist plots at each potential domain determined from Fig. 1 and their corresponding SEM images; A: -1.70 V vs. Hg/HgO, B: -0.80 V vs. Hg/HgO and C: -1.20 V vs. Hg/HgO. Arrows are indicating frequency values (Hz).

Fig. 3. AESEC-EIS curve of $Al_{5.2}Zn$ in 0.1 M NaOH, Ar deaerated electrolyte including potentiostatic hold (E_{ap}), EIS and open circuit measurement (E_{oc}). **A**: E_{ap} = -1.70 V vs. Hg/HgO, **B**: E_{ap} = -0.80 V vs. Hg/HgO and **C**: E_{ap} = -1.20 V vs. Hg/HgO. j_M (M = Zn or Al) values are normalized based on the molar composition for **B** and **C**.

Fig. 4. The oscillation trends at low frequency domain for A: E_{ap} = -0.80 V vs. Hg/HgO and B: E_{ap} = -1.20 V vs. Hg/HgO from Figs. 3B and 3C, respectively.

Fig. 5. Lissajous analysis at f = 0.004 Hz at A: E_{ap} = -0.80 V vs. Hg/HgO and B: E_{ap} = -1.20 V vs. HgO. The j_e^*, j_{Al} and j_{Zn} are shown as a function of IR drop compensated applied potential ($E-j_eR_e$). One cycle including upper and lower potential scans, indicated by arrows, is given.

Fig. 6. Simplified schematic model of elemental dissolution at each interface of Al_xZn in 0.1 M NaOH solution in anodic potential domain.

Fig. 7. A: AESEC-EIS curve of Zn-22 wt.% Al in 0.1 M NaOH, Ar deaerated electrolyte, at E_{ap} = -1.36 V vs. Hg/HgO, **B**: Oscillation trends at f = 0.010 Hz, and **C**: Corresponding Nyquist plot.

Table 1. The effective capacitance values obtained from Brug's relation [18] **(a)**, complex capacitance curve [15] **(b)** and **(c)**. CPE parameters (α and Q) are provided. The corresponding

effective oxide layer thickness (δ) calculated by Eq. 5 and obtained from the AESEC mass-balance are given.

	E_{ap} / V vs. Hg/HgO	C / μF cm^{-2}	α	Q / Ω^{-1} cm^{-2} s$^{\alpha-1}$	Effective thickness (δ) / nm	
					EIS	AESEC
(a)	-1.70 V	C_{dl} = 191	0.73	(1.07 ± 0.20) x 10^{-3}	-	
(b)	-0.80 V	C_{δ} = 0.65	0.78	(12.6 ± 0.2) x 10^{-4}	12 ± 1	11
(c)	-1.20 V	C_{δ} = 3.3	0.77	(4.5 ± 1.3) x 10^{-5}	2.4 ± 0.3	2.5

Table 2. The real part impedance measured by the potentiostat (Z_r - Z_e), contribution of Zn dissolution ($Z_r(j_{Zn})$) and Al dissolution (Z_r (j_{Al})).

f / Hz	Z_r - Z_e / Ω cm^2	Z_r (j_{Zn}) / Ω cm^2	Z_r (j_{Al}) / Ω cm^2
E_{ap} = -0.80 V vs. Hg/HgO (anodic domain)			
0.010	194	878	19
0.004	192	872	61
E_{ap} = -1.20 V vs. Hg/HgO (intermediate domain)			
0.013	305	270	48
0.010	297	274	37
0.008	287	275	37
0.006	279	234	29
0.004	275	266	34

518 **Table 3.** The real part of impedance, and ϕ obtained from Fig. 7.

f / Hz	$(Z_r - Z_e)$ / Ω cm^2	Z_r (j_{Zn}) / Ω cm^2	Z_r (j_{Al}) / Ω cm^2	ϕ (E vs. j_e)
0.013	101	61	67	-29˚
0.010	103	67	75	-32˚
0.007	110	66	28	-63˚

519

520 **References**

[1] Epelboin, I., Keddam, M., & Takenouti, H. Use of impedance measurements for the determination of the instant rate of metal corrosion. *J. Applied Electrochem.* **2,** 71-79 (1972).

[2] Keddam, M., Mattos, O.R. & Takenouti, H. Mechanism of anodic dissolution of iron-chromium alloys investigated by electrode impedances - II. Elaboration of the reaction model. *Electrochim. Acta,* **31,** 1159-1165 (1986).

[3] Wang, X. et al. A new transfer function in electrochemistry: Dynamic coupling between Raman spectroscopy and electrochemical impedance spectroscopy. *Electrochim. Acta,* **55,** 6299-6307 (2010).

[4] Gabrielli, C. & Tribollet, B. A Transfer Function Approach for a Generalized Electrochemical Impedance Spectroscopy. *J. Electrochem. Soc.* **141,** 1147-1157 (1994).

[5] Ogle, K. Atomic emission spectroelectrochemistry: Real time rate measurements of dissolution, corrosion and passivation. *Corrosion*, **75**(12), 1398-1419 (2019).

[6] Jiang, L., Wolpers, M., Volovitch, P. & Ogle, K. The degradation of phosphate conversion coatings by electrochemically generated hydroxide. *Corros. Sci.* **55**, 76-89 (2012).

[7] Jiang, L., Wolpers, M., Volovitch, P. & Ogle, K. An atomic emission spectroelectrochemical study of passive film formation and dissolution on galvanized steel treated with silicate conversion coating. *Surf. & Coat. Tech.* **206**, 3151-3157 (2012).

[8] Shkirskiy, V., & Ogle, K. A novel coupling of electrochemical impedance spectroscopy with atomic emission spectroelectrochemistry: Application to the open circuit dissolution of zinc. *Electrochim. Acta*, **168**, 167-172 (2015).

[9] Vu, T. N., Volovitch, P. & Ogle, K. The effect of pH on the selective dissolution of Zn and Al from Zn–Al coatings on steel. *Corros. Sci.* **67,** 42-49 (2013).

[10] Vu, T. N., Mokaddem, M., Volovitch, P. & Ogle, K. The anodic dissolution of zinc and zinc alloys in alkaline solution. II. Al and Zn partial dissolution from 5% Al–Zn coatings. *Electrochim. Acta*, **74**, 130–138 (2012).

[11] Han, J. & Ogle, K., Cathodic dealloying of α-phase Al-Zn in slightly alkaline chloride electrolyte and its consequence for corrosion resistance. *J. Electrochem. Soc.* **165**, C334-C342 (2018).
[12] Han, J. & Ogle, K. The anodic and cathodic dissolution of α-phase Zn-68Al in alkaline media. *Corros. Sci.* **148**, 1-11 (2019).
[13] Han, J., Thierry, D. & Ogle, K. Temperature dependence of the passivation and dissolution of Al, Zn and α-phase Zn-68Al. *Corrosion*, **75**(1), 68-78 (2019).
[14] Han, J. & Ogle, K. Hydrogen evolution and elemental dissolution by combined gravimetric method and atomic emission spectroelectrochemistry. *J. Electrochem. Soc.* **166**(11), C3068-3070 (2019).
[15] Benoit, M. et al. Comparison of different methods for measuring the passive film thickness on metals. *Electrochem. Acta*, **201**, 340-347 (2016).
[16] Orazem, M. E., Pébère, N. & Tribollet, B. Enhanced graphical representation of electrochemical impedance data. *J. Electrochem. Soc.* **153**(4), B129-B139 (2006).
[17] Hirschorn, B. et al. Determination of effective capacitance and film thickness from constant-phase-element parameters. *Electrochim. Acta*, **55**, 6218-6227 (2010).
[18] Brug, G. J., Van Den Eeden, A. L. G., Sluyters-Rehbach, M. & Sluyters, J. H. The analysis of electrode impedance complicated by the presence of a constant phase element. *J. Electroanal. Chem.* **176**, 275-295 (1984).
[19] Zhang, J., Klasky, M. & Letellier, B. C. The aluminum chemistry and corrosion in alkaline solutions. *J. Nucl. Mater.* **384**, 175-189 (2009).

[20] Chu, D. & Savinell, R.F. Experimental data on aluminum dissolution in KOH electrolytes. *Electrochim. Acta*, **36**(10) 1631-1638 (1991).
[21] Moon, S. M. & Pyun, S. I. The corrosion of pure aluminium during cathodic polarization in aqueous solutions. *Corros. Sci.* **39**(2) 399-408 (1997).

[22] Pyun, S. & Moon, S. Corrosion mechanism of pure aluminium in aqueous solution", *J. Solid State Electrochem.* **4**, 267-272 (2000).
[23] Cachet, C. Ströder, U. & Wiart, R. The kinetics of zinc electrode in alkaline zincate electrolytes. *Electrochim. Acta*, **27**(7), 903-908 (1982).

[24] Cachet, C., De Pauli, C. P. & Wiart, R. The passivation of zinc in slightly alkaline solutions. *Corros. Sci.* **25**(7), 493-502 (1985).
[25] Hirschorn, B. et al. Constant-phase-element behavior caused by resistivity distributions in films: II. Applications. *J. Electrochem. Soc.* **157**(12), C458-C462 (2010).
[26] Hirschorn, B. et al. Constant-phase-element behavior caused by resistivity distributions in films: I. Theory. *J. Electrochem. Soc.* **157**(12), C452-C457 (2010).
[27] Madelung, O., Rössler, U., & Schulz M. (eds) II-VI and I-VII Compounds; Semimagnetic compounds. Landolt-Börnstein – Group III Condensed Matter (Numerical data and functional relationships in science and technology), vol. 41B. Springer, Berlin, Heidelberg.
[28] Shkirskiy, V., Maltseva, A., Ogle, K. & Volovitch, P. Environmental effects on selective dissolution from ZnAlMg alloy under low frequency alternating current perturbations. *Electrochim. Acta*, **238**, 397-409 (2017).
[29] Bockris, J. O'M., Nagy, Z. & Damjanovic, A. On the deposition and dissolution of zinc in alkaline solutions. *J. Electrochem. Soc.* **119**(3), 285-295 (1975).

[30] Cachet, C., Saïdani, B. & Wiart, R. The behavior of zinc electrode in alkaline electrolytes I. A kinetic analysis of cathodic deposition. *J*. *Electrochem*. *Soc*. **138**(3), 678-687 (1991).
[31] Thomas, S., Birbilis, N., Venkatraman, M. S. & Cole, I. S. Corrosion of zinc as a function of pH. *Corrosion*, **68**(1), 015009-1 (2012).
[32] Armstrong, R. D. & Bell, M. F. The active dissolution of zinc in alkaline solution. *Electroanal*. *Chem*. *& Interf*. *Electrochem*. **55**, 201-211 (1974).
[33] de Wit, J. H. W., & Lenderink, H. J. W. Electrochemical impedance spectroscopy as a tool to obtain mechanistic information on the passive behaviour of aluminium. *Electrochim*. *Acta*, **41**(7-8), 1111-1119 (1996).
[34] Lnderink, H. J. W., Linden, M. V. D. & de Wit, J. H. W. Corrosion of aluminium in acidic and neutral solutions. *Electrochim*. *Acta*, **38**(14), 1989-1992 (1993).
[35] Gudić, S., Radošević, J. & Kliškić, M. Study of passivation of Al and Al–Sn alloys in borate buffer solutions using electrochemical impedance spectroscopy. *Electrochim*. *Acta*, **47,** 3009-3016 (2002).
[36] Han, J. The electrochemistry and dealloying of Zn-Mg/Zn-Al pure phases and their significance for corrosion of Zn-Al-Mg alloys. Ph.D. thesis, Chimie ParisTech (2018).
[37] Epelboin, I., Keddam, M. & Lestrade, J. C. Faradaic impedances and intermediates in electrochemical reactions. *Faraday Discuss*. *Chem*. *Soc*. **56**, 264-275 (1973).
[38] Annergren, I., Keddam, M., Takenouti, H. & Thierry, D. Modeling of the passivation mechanism of Fe-Cr binary alloys from ac impedance and frequency resolved rrde-I. Behavior of Fe-Cr alloys in 0.5 M H_2SO_4. *Electrochim*. *Acta*, **41**, 1121-1135 (1996).
[39] Stoulil, J. et al. Electrochemical properties of corrosion products formed on Zn-Mg, Zn-Al and Zn-Al-Mg coatings in model atmospheric conditions. *Mat*. *& Corros*. **66**(8), 777-782 (2015).
[40] Ogle, K. & Weber, S. Anodic dissolution of 304 stainless steel using atomic emission spectroelectrochemistry. *J*. *Electrochem*. *Soc*. **147**(5), 1770-1780 (2000).
[41] Lodi, P., Ogle, K. & Storhaye, A. Méthode d'analyse d'un échantillon métallique par dissolution de sa surface, et dispositif pour sa mise en œuvre. Patent, 92-3782, France (1992).